Boundary-driven nonequilibrium gas flow in a grooved channel via kinetic theory

Steryios Naris and Dimitris Valougeorgis[a)]
Department of Mechanical and Industrial Engineering, University of Thessaly, Pedion Areos, Volos 38334, Greece

(Received 16 January 2007; accepted 5 April 2007; published online 12 June 2007)

The nonequilibrium flow of a gas in a two-dimensional grooved channel, due to the motion of the wall of the channel, is investigated based on kinetic theory. The presence of the rectangular grooves that are placed periodically on the stationary wall results in a two-dimensional flow pattern. The problem is modeled by the linearized Bhatnagar-Gross-Krook (BGK) and S-model kinetic equations, which are solved for the corresponding perturbed distribution functions by the discrete velocity method. Maxwell diffuse type reflecting boundary conditions are used to model the gas-surface interaction, while periodic boundary conditions are imposed at the inlet and outlet of the channel. The computed macroscopic quantities of practical interest include velocity profiles, contours of pressure, density, and temperature, as well as the flow rate and the heat flux through the channel and the drag coefficient along the moving boundary. The results are valid in the whole range of the Knudsen number, from the free molecular regime through the transition and slip regimes up to the hydrodynamic limit, for various values of the depth and the width of the groove and the periodic length of the channel. A comparison between the BGK and S-model results is performed. Several interesting flow patterns and characteristics are examined in terms of the geometrical parameters of the flow configuration, including an unexpected behavior of the velocity profile across the channel at large Knudsen numbers. © *2007 American Institute of Physics*.
[DOI: 10.1063/1.2739414]

I. INTRODUCTION

The field of nonequilibrium flows is considered as one of the most challenging frontiers in fluid mechanics and transport phenomena, with many applications in nano- and microdevices, vacuum technology, and high altitude aeronautics.[1] Whether the flow is in equilibrium is determined by the Knudsen number, which is defined as the ratio of the mean free path over a characteristic macroscopic length of the problem.

One of the nonequilibrium flow configurations, which is very common in several engineering and technological fields, is the flow of a rarefied gas through a grooved channel. This type of flow may be considered as a prototype flow for more complicated flow patterns, and its detailed investigation is a topic of recent interest. In microfluidics, a two-dimensional boundary-driven flow in a grooved channel has been considered in order to model the flow complexity in micromotors and microbearings or the coolant flow over circuit boards in electronic microdevices.[2,3] In an effort to enhance mixing in microchannels, various patterned grooved configurations have been investigated in Ref. 4. In other occasions, the effect of the surface roughness in microchannel flows has been modeled by placing grooves of several shapes and sizes along the surfaces.[5,6] In vacuum systems, modeling of pumps operating at very low densities requires the solution of rarefied flows through grooved channels, where the grooved plate corresponds to the spiral grooved stator and the flat plate to the rotor.[7–9] Finally, in aeronautics, surface microgrooves have been used in several high-speed applications including near-wall exergy and flow control with applications to aircraft intake deicing.[10]

In all previously mentioned work, the flow is simulated by implementing the Navier-Stokes equations subject to slip boundary conditions[2] or by the direct simulation Monte Carlo (DSMC) method.[11] The first approach is limited by the continuum assumption, which is not valid as we depart far enough from equilibrium.[12] The second statistical type approach, although in most cases is a powerful computational tool, in the case of flows characterized by low Mach and Reynolds numbers may deduce inaccurate results due to statistical noise.

An alternative and very reliable approach for solving nonequilibrium flows in the whole range of the Knudsen number is the kinetic approach based on the Boltzmann equation or alternatively on reliable kinetic model equations.[13–16] During recent years it has been shown that kinetic solutions based on the corresponding linearized model equations, which are solved by implementing upgraded versions of the discrete velocity method,[17,18] are particularly suitable for slow flows providing very accurate results with modest computational effort.[19–21]

The investigation of rarefied gas flows through grooved channels via kinetic theory is limited. In an effort to model a pump without moving parts, known as the Knudsen pump, the gas flow through a grooved channel caused by a periodic wall temperature distribution has been studied in Ref. 22 and

[a)]Author to whom correspondence should be addressed. Electronic mail: diva@mie.uth.gr

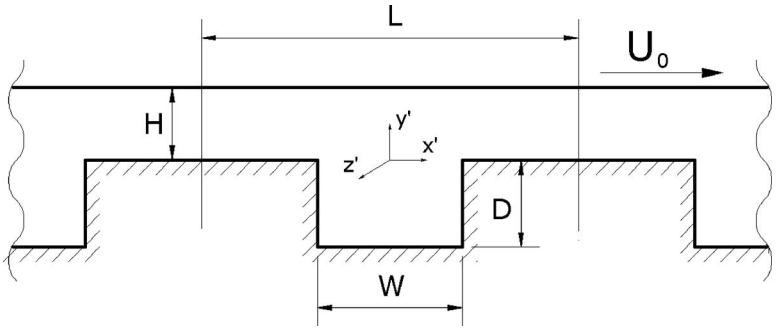

FIG. 1. Grooved channel geometry.

more recently in Refs. 23 and 24. Also, the flow of a rarefied gas through a grooved channel due to pressure and temperature gradients in the longitudinal direction has been investigated by the BGK model in Ref. 25 and by the S model in Ref. 26. For boundary-driven flow of a rarefied gas in a grooved channel, as far as we are aware, the only kinetic type investigation has been reported very recently in an effort to model the Holweck vacuum pump.[27] In that work, the main objective was the estimation of certain design parameters of the pump and therefore only the overall quantities of the flow rate and the drag coefficient are reported without a detailed description of the flow patterns and characteristics, as well as of the macroscopic distributions, such as velocities and pressures.

Overall, it is noted that the boundary-driven flow of a rarefied gas in a grooved channel, over the whole range of the Knudsen number, which is of particular interest in several fields, has not been thoroughly investigated and more detailed work is needed. In addition to their practical applications, nonequilibrium grooved flows contain several flow and transport phenomena of theoretical interest. In continuum (equilibrium) fluid mechanics, this type of flow has been extensively investigated.[28,29]

In the present work, a detailed investigation is provided for the two-dimensional steady-state flow of a rarefied gas in a periodically grooved channel, based on the linearized BGK and S equations. The flow is due to the motion of the smooth wall of the channel. A methodology recently introduced in the solution of the nonequilibrium cavity problem[30] is extended to solve numerically the present flow configuration. The approach is applicable in the whole range of gas rarefaction, deducing accurate results from the free molecular regime through the transition and slip regimes up to the hydrodynamic limit, for various values of the aspect ratio of the groove and the periodic length of the channel. Due to the applied linearization, the analysis is valid for small Mach and Reynolds numbers.

II. FORMULATION OF THE PROBLEM

A. Flow configuration

The geometry of the periodically grooved channel to be considered, with the coordinate system and its origin, is shown in Fig. 1. The channel consists of two parallel plates, assumed infinite in extent in the x' and z' directions and separated by a distance H, measured in the y' direction. The upper plate is flat, while the lower one has a series of rectangular grooves uniformly distributed. The cross section of each groove is $W \times D$, where W and D denote the width and the depth of the groove, respectively. It is assumed that the geometry repeats itself with a period L.

Next, consider the flow of a rarefied gas between the two plates of the channel, where the lower plate is stationary while the upper one is moving with constant velocity U_0. The flow is considered as unbounded in the z' direction and end effects in that direction are neglected. It is obvious that there is a resemblance, in terms of the driving mechanism and the expecting flow characteristics and properties, to the classical one-dimensional Couette flow problem. However, here the presence of the rectangular grooves that are placed periodically along the stationary wall results in a two-dimensional flow pattern. The flow depends on both x' and y', with x' being the streamwise direction. Due to the imposed periodicity, only one section with length L of the grooved channel may be considered.[25,27] The flow domain under investigation is bounded by the flow inlet and outlet boundaries at $x'=-L/2$ and $L/2$, respectively, and by the top and bottom walls. All the walls are considered isothermal with temperature T_0. By taking the distance H between the plates as the characteristic length of the problem, the nondimensional spatial variables are $x=x'/H$, $y=y'/H$, and $z=z'/H$.

B. Basic equations

The basic parameter of this nonequilibrium flow is the Knudsen number. For practical purposes, however, we choose to present our methodology and results in terms of the so-called gas rarefaction parameter, which is defined as

$$\delta = \frac{HP_0}{\mu_0 v_0} = \frac{\sqrt{\pi}}{2}\frac{1}{\mathrm{Kn}}. \tag{1}$$

Here, H is the characteristic macroscopic length, P_0 is the reference pressure, considered at the inlet of the channel, μ_0 is the gas viscosity at temperature T_0, and $v_0=\sqrt{2RT_0}$ is the characteristic molecular velocity, with $R=k/m$ denoting the gas constant (k is the Boltzmann constant and m is the molecular mass). As is seen, the rarefaction parameter δ is defined in terms of measurable quantities and it is proportional to the inverse Knudsen number.

The flow under consideration is stationary and does not depend on the spanwise z direction. Since a kinetic approach is followed, the basic unknown is the distribution function $f=f(x,y,\boldsymbol{c})$, where x and y have been defined earlier and

$\boldsymbol{c}=(c_x,c_y,c_z)$ is the nondimensional molecular velocity vector, while the macroscopic quantities are obtained by the moments of f. The gas pressure, density, and temperature are related by the equation of state $P(x,y)=n(x,y)RT(x,y)$. The equilibrium state is perturbed by the motion of the upper wall with velocity $U_0 \ll v_0$. Then, the flow may be linearized by introducing the relation

$$f = f^0\left[1 + h\frac{U_0}{v_0}\right], \tag{2}$$

where $h=h(x,y,\boldsymbol{c})$ is the new unknown function and

$$f^0 = \frac{n_0}{(2\pi RT_0)^{3/2}}e^{-c^2} \tag{3}$$

is the global (absolute) equilibrium distribution function defined at the reference number density n_0 and temperature T_0.

We intend to find the unknown distribution function $h=h(x,y,\boldsymbol{c})$ by implementing both the BGK and the S kinetic models. Usually the BGK equation is used in isothermal flows, while the S model, due to its ability to provide simultaneously correct expressions for both the viscosity and the thermal conductivity coefficients, is used in nonisothermal flows. In the present case, although the walls are isothermal, there is a temperature variation in the field. Therefore, we implement both models in order to compare the corresponding solutions and to decide on their applicability and validity in this particular problem. In addition, the S-model solution will be useful, when the present flow configuration will be extended in future work to the case of binary gas mixtures. To distinguish the two solutions, we denote the unknown distribution functions by $h^{(k)}$, with $k=1$ and 2 denoting the solutions of the BGK and S models, respectively.

The flow may be described by the two-dimensional steady-state BGK[31,32] and S[33] kinetic equation given by

$$c_x\frac{\partial h^{(1)}}{\partial x} + c_y\frac{\partial h^{(1)}}{\partial y} + \delta h^{(1)} = \delta\left[\rho^{(1)} + 2c_x u_x^{(1)} + 2c_y u_y^{(1)} + \tau^{(1)}\left(c^2 - \frac{3}{2}\right)\right] \tag{4}$$

and

$$c_x\frac{\partial h^{(2)}}{\partial x} + c_y\frac{\partial h^{(2)}}{\partial y} + \delta h^{(2)} = \delta\left[\rho^{(2)} + 2c_x u_x^{(2)} + 2c_y u_y^{(2)} + \tau^{(2)}\left(c^2 - \frac{3}{2}\right) + \frac{4}{15}(c_x q_x^{(2)} + c_y q_y^{(2)})\left(c^2 - \frac{5}{2}\right)\right], \tag{5}$$

respectively. The nondimensional perturbed macroscopic distributions of number density, velocity, temperature, and heat flux on the right-hand side of Eqs. (4) and (5) are deduced by the moments of $h^{(k)}$, with $k=1,2$ according to

$$\rho^{(k)}(x,y) = \frac{1}{\pi^{3/2}}\int_{-\infty}^{\infty} h^{(k)}e^{-c^2}d\boldsymbol{c}, \tag{6}$$

$$\boldsymbol{u}^{(k)}(x,y) = \frac{1}{\pi^{3/2}}\int_{-\infty}^{\infty} \boldsymbol{c}h^{(k)}e^{-c^2}d\boldsymbol{c}, \tag{7}$$

$$\tau^{(k)}(x,y) = \frac{1}{\pi^{3/2}}\int_{-\infty}^{\infty} \left(\frac{2}{3}c^2 - 1\right)h^{(k)}e^{-c^2}d\boldsymbol{c}, \tag{8}$$

and

$$\boldsymbol{q}^{(k)}(x,y) = \frac{1}{\pi^{3/2}}\int_{-\infty}^{\infty} \boldsymbol{c}\left(c^2 - \frac{5}{2}\right)h^{(k)}e^{-c^2}d\boldsymbol{c}, \tag{9}$$

respectively, where $\int_{-\infty}^{\infty}(\cdots)d\boldsymbol{c}=\int_{-\infty}^{\infty}\int_{-\infty}^{\infty}\int_{-\infty}^{\infty}(\cdots)dc_x dc_y dc_z$. Other macroscopic quantities of some interest for this problem are the nondimensional shear stress given by

$$\omega^{(k)}(x,y) = \frac{1}{\pi^{3/2}}\int_{-\infty}^{\infty} c_x c_y h^{(k)}e^{-c^2}d\boldsymbol{c} \tag{10}$$

and the nondimensional pressure defined as

$$p^{(k)}(x,y) = \frac{P^{(k)} - P_0}{P_0} = \tau^{(k)} + \rho^{(k)}. \tag{11}$$

Equation (11) is the linearized equation of state.

It turns out, as discussed in Sec. IV, that in this flow configuration the temperature perturbation is one order of magnitude less compared to the density and pressure perturbations, which are of the same order, and therefore it may be neglected. However, this is not known from the beginning and must be examined. In addition, the analysis is more complete and accurate and more easily extended to the nonisothermal grooved channel flow.

Finally, we define the following three overall macroscopic quantities. First, by integrating the shear stress, given by Eq. (10), along the top flat plate we estimate the drag coefficient,

$$C_d^{(k)} = \frac{2}{L}\int_{-L/2H}^{L/2H} \omega^{(k)}(x,1)dx \tag{12}$$

at the upper boundary. Second, by integrating across the inlet of the channel the x component of the velocity profile, given by Eq. (7), we find the nondimensional flow rate,

$$G^{(k)} = 2\int_0^1 u_x^{(k)}\left(-\frac{L}{2H},y\right)dy. \tag{13}$$

It is obvious that integrating at any cross section of the channel, the corresponding x component of the velocity profile will result in the same flow rate. Third, by integrating the x component of the heat flux, given by Eq. (9), over the whole computational domain, we compute the nondimensional average heat flux,

$$Q^{(k)} = 2\frac{H}{L}\int\int q_x^{(k)}(x,y)dydx. \tag{14}$$

It is noted that the average heat flux at each cross section of the channel is not constant and therefore we choose to compute the average heat flux Q in the whole channel.

For the boundary-driven problem, the drag coefficient is considered as a direct effect, while the flow rate and the heat

flux are considered as cross effects. In Sec. IV, we estimate these three quantities for the present flow configuration and then we compare them with the corresponding ones for the classical one-dimensional Couette flow problem in order to have an overall quantitative description of the effect of the groove in the flow.

C. Reduced BGK kinetic equations

For the problem under consideration, taking advantage of the two-dimensionality of the flow, the c_z component of the molecular velocity vector may be eliminated from both model equations by following the well-known projection procedure. Equations (4) and (5) are multiplied successively by $\frac{1}{\sqrt{\pi}}e^{c_z^2}$ and by $\frac{1}{\sqrt{\pi}}(c_z^2-1/2)e^{c_z^2}$ and the resulting equations are integrated over all $-\infty<c_z<\infty$. Of course, by doing that we obtain for each model a set of two equations. However, the deduced equations after the projection do not contain the variable c_z, and the computational effort associated with the implemented discrete velocity method, discussed in the next section, is significantly reduced.

Even more, for computational purposes it is convenient to express the two remaining components c_x and c_y of the particle velocity in terms of polar coordinates. The two-component dimensionless molecular velocity vector is now defined by its magnitude μ and its polar angle θ given by

$$\mu=\sqrt{c_x^2+c_y^2} \quad \text{and} \quad \theta=\tan^{-1}\left(\frac{c_y}{c_x}\right), \tag{15}$$

respectively, where $0\leqslant\mu<\infty$ and $0\leqslant\theta\leqslant 2\pi$. In addition, using polar coordinates in the molecular velocity space, we may write the linear differential operator acting on the distribution functions on the left-hand side of Eqs. (4) and (5) in the more convenient form

$$c_x\frac{\partial}{\partial x}+c_y\frac{\partial}{\partial y}=\mu\left[\cos\theta\frac{\partial}{\partial x}+\sin\theta\frac{\partial}{\partial y}\right]=\mu\frac{d}{ds}. \tag{16}$$

Here s denotes the direction of the characteristic defined by the polar angle θ of the molecular velocity vector.

Based on the above discussion, we define the reduced distribution functions

$$\phi^{(k)}(x,y,\mu,\theta)=\frac{1}{\sqrt{\pi}}\int_{-\infty}^{\infty}h^{(k)}(x,y,\mu,\theta,c_z)e^{-c_z^2}dc_z \tag{17}$$

and

$$\psi^{(k)}(x,y,\mu,\theta)=\frac{1}{\sqrt{\pi}}\int_{-\infty}^{\infty}h^{(k)}(x,y,\mu,\theta,c_z)\left(c_z^2-\frac{1}{2}\right)e^{-c_z^2}dc_z, \tag{18}$$

with $k=1,2$, and we operate accordingly on Eqs. (4) and (5) to deduce, after some routine manipulation, the reduced model equations. In particular, the BGK model is described by

$$\mu\frac{d\phi^{(1)}}{ds}+\delta\phi^{(1)}=\delta[\rho^{(1)}+2\mu(u_x^{(1)}\cos\theta+u_y^{(1)}\sin\theta)+\tau^{(1)}(\mu^2-1)] \tag{19}$$

and

$$\mu\frac{d\psi^{(1)}}{ds}+\delta\psi^{(1)}=\delta\frac{\tau^{(1)}}{2}, \tag{20}$$

while the S model is described by

$$\mu\frac{d\phi^{(2)}}{ds}+\delta\phi^{(2)}=\delta\left[\rho^{(2)}+2\mu(u_x^{(2)}\cos\theta+u_y^{(2)}\sin\theta)+\tau^{(2)}(\mu^2-1)+\frac{4}{15}(c_xq_x^{(2)}+c_yq_y^{(2)})\times(\mu^2-2)\right] \tag{21}$$

and

$$\mu\frac{d\psi^{(2)}}{ds}+\delta\psi^{(2)}=\delta\left[\frac{\tau^{(2)}}{2}+\frac{2}{15}(c_xq_x^{(2)}+c_yq_y^{(2)})\right]. \tag{22}$$

Finally, by applying the corresponding reduction procedure to the nondimensional macroscopic quantities, given by Eqs. (6)–(10), we find

$$\rho^{(k)}(x,y)=\frac{1}{\pi}\int_0^{2\pi}\int_0^{\infty}\phi^{(k)}\mu e^{-\mu^2}d\mu d\theta, \tag{23}$$

$$u_x^{(k)}(x,y)=\frac{1}{\pi}\int_0^{2\pi}\int_0^{\infty}\phi^{(k)}\mu^2e^{-\mu^2}\cos\theta d\mu d\theta, \tag{24}$$

$$u_y^{(k)}(x,y)=\frac{1}{\pi}\int_0^{2\pi}\int_0^{\infty}\phi^{(k)}\mu^2e^{-\mu^2}\sin\theta d\mu d\theta, \tag{25}$$

$$\tau^{(k)}(x,y)=\frac{1}{\pi}\int_0^{2\pi}\int_0^{\infty}\frac{2}{3}[(\mu^2-1)\phi^{(k)}+\psi^{(k)}]\mu e^{-\mu^2}d\mu d\theta, \tag{26}$$

$$q_x^{(k)}(x,y)=\frac{1}{\pi}\int_0^{2\pi}\int_0^{\infty}[(\mu^2-2)\phi^{(k)}+\psi^{(k)}]\times\mu^2e^{-\mu^2}\cos\theta d\mu d\theta, \tag{27}$$

$$q_y^{(k)}(x,y)=\frac{1}{\pi}\int_0^{2\pi}\int_0^{\infty}[(\mu^2-2)\phi^{(k)}+\psi^{(k)}]\times\mu^2e^{-\mu^2}\sin\theta d\mu d\theta, \tag{28}$$

and

$$\omega^{(k)}(x,y)=\frac{1}{\pi}\int_0^{2\pi}\int_0^{\infty}\phi^{(k)}\mu^3e^{-\mu^2}\sin\theta\cos\theta d\mu d\theta, \tag{29}$$

with $k=1,2$.

The reduced model equations (19)–(22), with the associated integral expressions (23)–(28), are solved by a computational scheme, which is described in Sec. III.

D. Boundary conditions

We close our discussion on the formulation of the problem by determining the boundary conditions associated with the governing equations. Boundary conditions are imposed for the unknown distributions $h^{(k)}=h^{(k)}(x,y,\boldsymbol{c})$, $k=1,2$, at the inlet and the outlet of the flow domain as well as along the lower and upper plates (see Fig. 1), yielding a well-posed elliptic type problem.

The flow field is periodic in the x direction with period L. Then, the periodic boundary conditions at the inlet and the outlet of the flow field imply that

$$h^{(k)}\left(-\frac{L}{2H},y,\boldsymbol{c}\right)=h^{(k)}\left(\frac{L}{2H},y,\boldsymbol{c}\right). \tag{30}$$

On the wall boundaries, the gas-surface interaction is modeled by the Maxwell diffuse reflection condition. Applying linearization, we deduce

$$h^{(k)+}=n_w^{(k)}, \quad \boldsymbol{c}\cdot\boldsymbol{n}>0 \tag{31}$$

along the stationary wall and

$$h^{(k)+}=n_w^{(k)}+2c_x, \quad c_y<0 \tag{32}$$

along the moving wall. The superscript + denotes distributions leaving from the boundaries and the vector $\mathbf{n}$ is defined as the unit vector normal to the surfaces and pointing toward the flow. The parameters $n_w^{(k)}$ are estimated by satisfying the well-known impermeability condition $\mathbf{u}\cdot\mathbf{n}=0$ along the walls of the channel. The second term on the right-hand side of Eq. (32) is due to the motion of the upper wall and it is the only nonhomogeneous term in the problem producing the flow. The velocity U_0 does not appear due to the imposed linearization [Eq. (2)] and also due to the fact that all quantities are in nondimensional form.

The boundary conditions for the reduced kinetic equations (19)–(22) are obtained in a straightforward manner. The projection procedure is applied to Eqs. (30)–(32) followed by the change of the microscopic velocity variables from Cartesian to polar coordinates. Then, the periodic boundary conditions are

$$\phi^{(k)}\left(-\frac{L}{2H},y,\mu,\theta\right)=\phi^{(k)}\left(\frac{L}{2H},y,\mu,\theta\right) \tag{33}$$

and

$$\psi^{(k)}\left(-\frac{L}{2H},y,\mu,\theta\right)=\psi^{(k)}\left(\frac{L}{2H},y,\mu,\theta\right), \tag{34}$$

while along the walls of the channel, we have

$$\phi^{(k)+}=n_w^{(k)} \quad \text{and} \quad \psi^{(k)+}=0, \quad \boldsymbol{c}\cdot\boldsymbol{n}>0 \tag{35}$$

on the stationary wall and

$$\phi^{(k)+}=n_w^{(k)}+2\mu\cos\theta \quad \text{and} \quad \psi^{(k)+}=0, \quad c_y<0 \tag{36}$$

on the moving wall. Again, the superscript + denotes leaving distributions and the parameters $n_w^{(k)}$ are defined by the no-penetration condition. In particular, at the three boundaries parallel to the x axis, we find

$$n_w^{(k)}\left(x,-\frac{D}{H}\right)=-\frac{2}{\sqrt{\pi}}\int_{\pi}^{2\pi}\int_0^{\infty}\phi^{(k)}\left(x,-\frac{D}{H},\mu,\theta\right)\times\mu^2e^{-\mu^2}\sin\theta d\mu d\theta,$$

$$-\frac{W}{2H}\leqslant x\leqslant\frac{W}{2H}, \tag{37}$$

$$n_w^{(k)}(x,0)=-\frac{2}{\sqrt{\pi}}\int_{\pi}^{2\pi}\int_0^{\infty}\phi^{(k)}(x,0,\mu,\theta)\mu^2e^{-\mu^2}\sin\theta d\mu d\theta,$$

$$\mp\frac{L}{2H}\leqslant x\leqslant\mp\frac{W}{2H} \tag{38}$$

and

$$n_w^{(k)}(x,1)=\frac{2}{\sqrt{\pi}}\int_0^{\pi}\int_0^{\infty}\phi^{(k)}(x,1,\mu,\theta)\mu^2e^{-\mu^2}\sin\theta d\mu d\theta,$$

$$-\frac{L}{2H}\leqslant x\leqslant\frac{L}{2H}, \tag{39}$$

while at the two boundaries parallel to the y axis we have

$$n_w^{(k)}\left(-\frac{W}{2H},y\right)=-\frac{2}{\sqrt{\pi}}\int_{3\pi/2}^{\pi/2}\int_0^{\infty}\phi^{(k)}\left(-\frac{W}{2H},y,\mu,\theta\right)\times\mu^2e^{-\mu^2}\cos\theta d\mu d\theta,$$

$$-\frac{D}{H}\leqslant y\leqslant 0 \tag{40}$$

and

$$n_w^{(k)}\left(\frac{W}{2H},y\right)=\frac{2}{\sqrt{\pi}}\int_{\pi/2}^{3\pi/2}\int_0^{\infty}\phi^{(k)}\left(\frac{W}{2H},y,\mu,\theta\right)\times\mu^2e^{-\mu^2}\cos\theta d\mu d\theta,$$

$$-\frac{D}{H}\leqslant y\leqslant 0. \tag{41}$$

Therefore, the unknown distribution functions $\phi^{(k)}$ and $\psi^{(k)}$ defined by Eqs. (19) and (20) for the BGK model and Eqs. (21) and (22) for the S model are subject to the boundary conditions (33)–(36).

III. THE COMPUTATIONAL SCHEME

The computational approach for solving the linear coupled integro-differential equations (19) and (20) for the BGK model and (21) and (22) for the S model, supplemented by the corresponding integral expressions (23)–(28) of the overall quantities, is presented. The procedure consists of splitting the initial problem into two subproblems and then solving the first one in a semianalytical manner, and the second one numerically in an iterative manner. Discretization in the phase space includes the discrete velocity method[15,34] and typical finite-difference schemes.

A. Splitting

The implemented splitting has been applied in the cavity flow problem.[30] This procedure eliminates only the propagation of the strong discontinuity induced by the motion of the upper plate, while the weak discontinuities are still there. In addition, one of the two subproblems is solved analytically only once. Here, we follow the same splitting procedure and we find again that it upgrades the whole numerical scheme producing accurate results free of oscillatory behavior with less computational effort.

The kinetic equations (19)–(22) are written in the more compact form,

$$\mu\frac{d\phi^{(k)}}{ds}+\delta\phi^{(k)}=\delta F^{(k)} \tag{42}$$

and

$$\mu\frac{d\psi^{(k)}}{ds}+\delta\psi^{(k)}=\delta Y^{(k)}, \tag{43}$$

with $k=1,2$, where $F^{(k)}$ and $Y^{(k)}$ are functionals representing the corresponding right-hand sides of the kinetic equations. Then, the unknown distributions $\phi^{(k)}$ are decomposed into two parts, namely

$$\phi^{(k)}=\phi_1^{(k)}+\phi_2^{(k)}. \tag{44}$$

Such a decomposition procedure is not necessary for the $\psi^{(k)}$ functions due to the fact that the associated boundary conditions are homogeneous and they do not contain source terms. Equation (44) is substituted into Eqs. (42) and the associated boundary conditions to yield the following two subproblems:

The first one is for $\phi_1^{(k)}$, described by the differential equation

$$\mu\frac{d\phi_1^{(k)}}{ds}+\delta\phi_1^{(k)}=0 \tag{45}$$

and the boundary conditions

$$\phi_1^{(k)+}=0 \tag{46}$$

at the stationary walls and

$$\phi_1^{(k)+}=2\mu\cos\theta \tag{47}$$

at the moving wall (the + sign denotes outgoing flux). This problem is solved analytically by integrating along the characteristics to yield

$$\phi_1^{(k)}(x,y,\mu,\theta)=\phi_1^{(k)+}e^{-\delta s_0/\mu}, \tag{48}$$

where s_0 is the distance along the characteristic line, in the direction opposite to that of the molecular velocity (μ,θ), from the point (x,y) to the boundary point where the characteristic is crossing the boundary (see Fig. 2). It is noted that Eq. (48) does not carry any discontinuity when it is applied in the main stream $(0<y<1)$ but it does carry the strong discontinuity due to the motion of the upper plate when it is applied inside the groove $(-D/H<y<0)$.

The second subproblem is for $\phi_2^{(k)}$ and it is described by the integro-differential equation

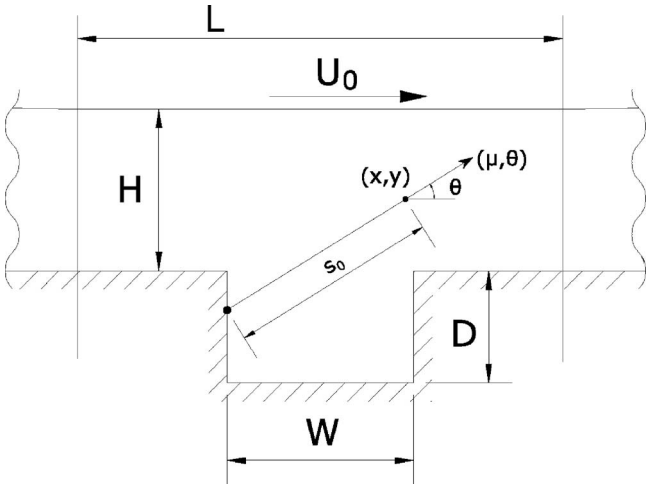

FIG. 2. Definition of distance s_0.

$$\mu\frac{d\phi_2^{(k)}}{ds}+\delta\phi_2^{(k)}=\delta F^{(k)} \tag{49}$$

with the boundary conditions

$$\phi_2^{(k)+}=n_w^{(k)} \tag{50}$$

at all surfaces (stationary and moving). The parameters $n_w^{(k)}$ are defined at the corresponding wall, by Eqs. (37)–(41).

Once the geometry of the problem is fixed, the distributions $\phi_1^{(k)}$ are estimated by Eq. (48) in a semianalytical manner. Then, the distributions $\phi_2^{(k)}$ and $\psi^{(k)}$ are computed by solving numerically, in an iterative manner, the coupled kinetic equations (49) and (43). In particular, the macroscopic equations on the right-hand side of the kinetic equations are assumed known and then the kinetic equations are solved for the unknown distributions $\phi_2^{(k)}$ and $\psi^{(k)}$. Based on these estimates and on the estimate of $\phi_1^{(k)}$, which already has been obtained, the macroscopic quantities are computed from the integral expressions and they are plugged back at the right-hand side of the kinetic equations. The iteration process is considered completed when the termination criteria imposed on the convergence of the overall quantities are satisfied. The discretization scheme is described in the next section.

B. Discretization in the phase space

The phase space consists of the molecular velocity and physical spaces. In the molecular velocity space, the discretization is performed by choosing a suitable set of discrete velocities (μ_m,θ_n), defined by $0\leqslant\mu_m<\infty$ and $0\leqslant\theta_n\leqslant2\pi$, with $m=1,2,\ldots,M$ and $n=1,2,\ldots,N$. The resulting set consists of $M\times N$ discrete velocities. The discretization in the physical space (x,y) is performed by dividing the flow domain in square elements and creating a typical physical grid. The nodes of the grid are denoted by (i,j), with $i=1,2,\ldots,I$ and $j=1,2,\ldots,J$.

Based on the above discretization, the unknown continuous functions $\phi^{(k)}(x,y,\mu,\theta)$ and $\psi^{(k)}(x,y,\mu,\theta)$ are substituted by the discretized quantities $\phi^{(k)}(x_i,y_j,\mu_m,\theta_n)=\phi_{i,j,m,n}^{(k)}=\phi_{1,i,j,m,n}^{(k)}+\phi_{2,i,j,m,n}^{(k)}$ and $\psi^{(k)}(x_i,y_j,\mu_m,\theta_n)=\psi_{i,j,m,n}^{(k)}$,

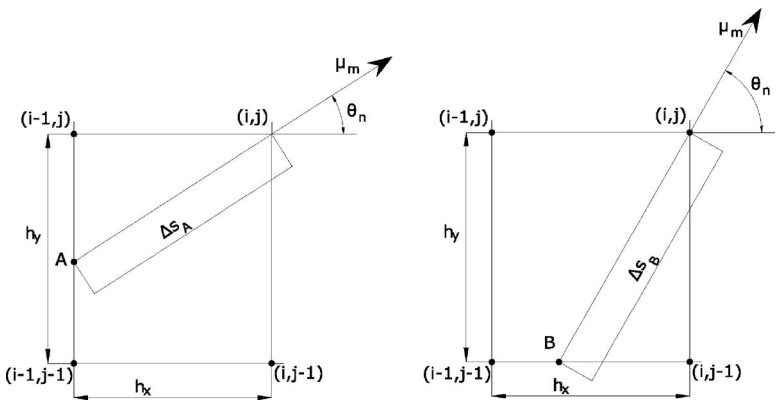

FIG. 3. Finite differencing of the first-order derivatives along a characteristic.

respectively. The first part of the $\phi^{(k)}$ functions can be readily deduced by discretizing accordingly the closed form expression (48). The estimation of $\phi^{(k)}_{1,i,j,m,n}$ requires only the computation of the distances s_0 at each grid point (x_i, y_j) and for each discrete polar angle θ_n. For this reason, we consider this solution as semianalytical. The estimation of $\phi^{(k)}_{2,i,j,m,n}$ and $\psi^{(k)}_{i,j,m,n}$ is achieved numerically by implementing the above described iteration scheme on the discretized equations. The integro-differential equations (49) and (43) are discretized first in the velocity space (μ_m, θ_n). By doing that, Eqs. (49) and (43) are deduced to a set of ordinary differential equations of the form

$$\mu_m \frac{d\phi^{(k)}_{2,m,n}}{ds} + \delta\phi^{(k)}_{2,m,n}(x,y) = \delta F^{(k)}(x,y) \tag{51}$$

and

$$\mu_m \frac{d\psi^{(k)}_{m,n}}{ds} + \delta\psi^{(k)}_{m,n}(x,y) = \delta Y^{(k)}(x,y), \tag{52}$$

respectively. Then, the system of ordinary differential equations (51) and (52) is discretized at each grid point (i,j) in the physical space yielding a set of algebraic equations. To achieve that, the first-order derivatives with respect to s in Eqs. (51) and (52) are approximated by a finite-difference first-order upwind scheme. For example, working in the first quadrant of the discrete molecular velocity space, with $0 < \theta_n < \pi/2$, we write

$$\frac{dg_{m,n}}{ds} = \frac{g_{i,j,m,n} - g_{A,m,n}}{\Delta s_A}, \quad \text{when} \quad 0 < \theta_n < \tan^{-1}\left(\frac{h_y}{h_x}\right) \tag{53}$$

and

$$\frac{dg_{m,n}}{ds} = \frac{g_{i,j,m,n} - g_{B,m,n}}{\Delta s_B}, \quad \text{when} \quad \tan^{-1}\left(\frac{h_y}{h_x}\right) < \theta_n < \frac{\pi}{2}, \tag{54}$$

where g denotes any of the two unknown distributions. The points A and B, with corresponding distances Δs_A and Δs_B, for a typical computational cell $h_x \times h_y$ are shown in Fig. 3. Then, the quantities at the points A and B are substituted by the corresponding quantities at the two adjacent grid points using linear interpolation. This approach can be easily extended for values of the polar angles θ_n at the remaining three quadrants. For each of the two models under investigation, there are $2 \times M \times N$ equations at each of the $I \times J$ nodes.

As has been pointed out, the whole problem is solved in an iterative manner between the kinetic equations and the integral expressions for the macroscopic quantities. However, at each iteration the system of algebraic equations can be solved by a marching scheme. For each discrete velocity (μ_m, θ_n) the distribution functions at each node are computed explicitly marching through the physical domain. Following this procedure, no matrix inversion is required. The macroscopic quantities, at each physical node (i,j), are computed by numerical integration. The Gauss-Hermite quadrature is used in the μ variable and the trapezoidal rule in the θ variable. The iterative procedure is ended when the imposed termination criteria on the convergence of the overall quantities are satisfied. Following the above procedure, supplemented by a reasonable dense grid and an adequate large set of discrete velocities, we are able to obtain grid-independent results with modest computational effort.

IV. RESULTS AND DISCUSSION

The solution depends on the rarefaction parameter δ, which defines the rarefaction of the flow and on the ratios D/H, W/H, and L/H, which define the geometry of the grooved channel. The effect of all these quantities on the solution of the problem has been investigated by carrying out detailed calculations for $0 \leqslant \delta \leqslant 10$, with $D/H = 0, 0.1, 0.3, 0.5, 1$, $W/H = 1, 2$, and $L/H = 2.5, 4$. The results for $D/H = 0$ correspond to the one-dimensional Couette flow problem.

The accuracy of the results depends on the discretization in the phase space (physical and molecular velocity spaces). In general, in rarefied atmospheres (small δ) we need a large number of discrete velocities, while the physical grid may be coarse. On the other hand, in continuum atmospheres (large δ) the required number of discrete velocities may be reduced, but dense physical grids are important to achieve good accuracy. Depending upon the value of δ and the geometry, the discretization has been progressively refined to ensure grid-independent results up to several significant figures. The presented results are with $h_x = h_y = 5 \times 10^{-3}$ in all cases, while the number of discrete velocities $M \times N$ is 64×400 for $\delta \leqslant 1$, 16×400 for $1 < \delta < 10$, and 16×200 for $\delta = 10$. Also, the

TABLE I. Drag coefficients and flow rates with the BGK model ($W/H=1$, $L/H=2.5$).

	D/H				
	1.0	0.5	0.3	0.1	0.0
δ			$C_d^{(1)}$		
0	0.609	0.621	0.620	0.592	0.564
10^{-3}	0.609	0.620	0.619	0.592	0.564
10^{-1}	5.557	0.567	0.566	0.544	0.522
1	0.346	0.350	0.350	0.344	0.339
10	0.811 (−1)	0.813 (−1)	0.814 (−1)	0.816 (−1)	0.831 (−1)
			$G^{(1)}$		
0	0.918	0.901	0.899	0.936	0.100 (1)
10^{-3}	0.918	0.901	0.899	0.936	0.100 (1)
10^{-1}	0.936	0.921	0.920	0.957	0.100 (1)
1	0.986	0.978	0.979	0.995	0.100 (1)
10	0.102 (1)	0.102 (1)	0.102 (1)	0.102 (1)	0.100 (1)

termination criterion on the convergence of the iterative process is set equal to 10^{-7}.

Tabulated results for the drag coefficient $C_d^{(k)}$ and the flow rate $G^{(k)}$ for five characteristic values of δ and for various values of D/H, with $W/H=1$ and $L/H=2.5$, are presented in Tables I and II based on the BGK and S models, respectively. The two models provide for these quantities identical results up to three significant figures. When the comparison is extended to the values of the heat flux $Q^{(k)}$, then the agreement is not as good. Overall, we have seen that both models provide identical results for the distributions of density, velocity, and shear stress and the overall quantities of drag coefficient and flow rate. When temperatures and heat fluxes are computed, then there is a departure in the results obtained by the two models, and in these cases, based on previous experience, the S-model results may be considered to be more accurate.

The results in the last column of Tables I and II ($D/H=0$), which have been obtained by implementing the present two-dimensional formulation and code, correspond to the solution of the one-dimensional Couette flow problem. They are in excellent agreement with the well known Couette flow results obtained by a typical one-dimensional discrete velocity code. This fact may be considered as a good benchmark regarding the accuracy of the present work.

It is seen, in Tables I and II, that for both computed quantities there is a departure of the one-dimensional results when $D/H\neq 0$. Even more, this departure is small for large values of δ and becomes more significant as δ is reduced, while for each δ the largest departure from the one-dimensional results seems to occur at $0.3\leqslant D/H\leqslant 0.5$. The qualitative behavior of the drag coefficient in terms of δ remains the same as in the typical Couette flow problem, and as expected the values of $C_d^{(k)}$ are reduced as δ is increased. However, the qualitative behavior of the flow rate is different since now it depends on δ and it is not constant and equal to 1 as in the case of the Couette flow. In particular, the values

TABLE II. Drag coefficients and flow rates with the S model ($W/H=1$, $L/H=2.5$).

	D/H				
	1.0	0.5	0.3	0.1	0.0
δ			$C_d^{(2)}$		
0	0.609	0.621	0.620	0.592	0.564
10^{-3}	0.609	0.620	0.619	0.592	0.564
10^{-1}	0.557	0.567	0.566	0.544	0.522
1	0.346	0.350	0.350	0.344	0.339
10	0.811 (−1)	0.813 (−1)	0.814 (−1)	0.816 (−1)	0.831 (−1)
			$G^{(2)}$		
0	0.918	0.901	0.899	0.936	0.100 (1)
10^{-3}	0.918	0.901	0.899	0.936	0.100 (1)
10^{-1}	0.936	0.920	0.920	0.957	0.100 (1)
1	0.986	0.978	0.979	0.995	0.100 (1)
10	0.102 (1)	0.102 (1)	0.102 (1)	0.102 (1)	0.100 (1)

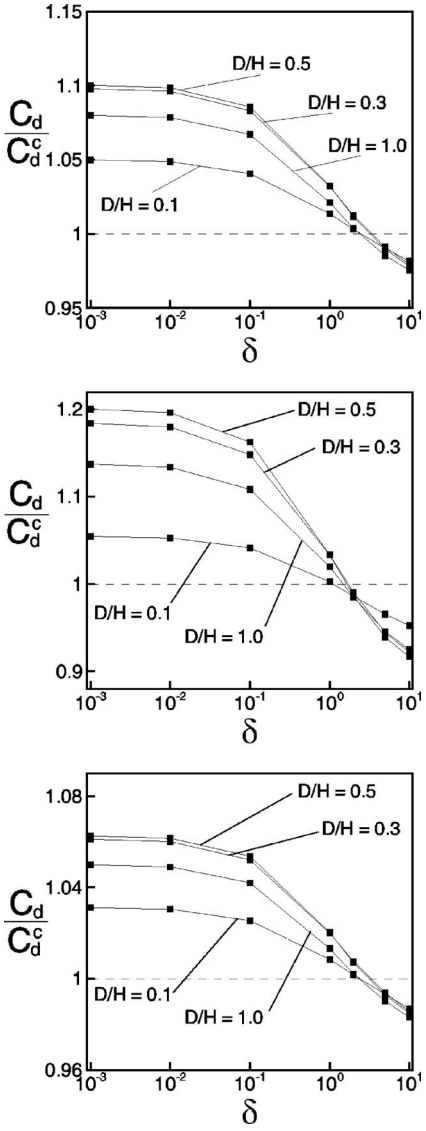

FIG. 4. Drag coefficient in terms of δ for various D/H with $W/H=1$, $L/H=2.5$ (top); $W/H=2$, $L/H=2.5$ (middle); and $W/H=1$, $L/H=4$ (bottom).

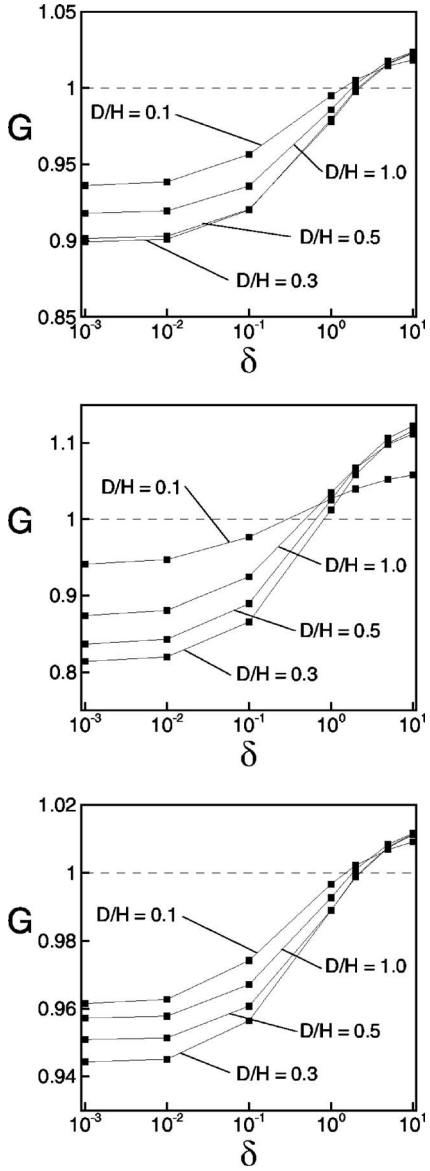

FIG. 5. Flow rate in terms of δ for various D/H with $W/H=1$, $L/H=2.5$ (top); $W/H=2$, $L/H=2.5$ (middle); and $W/H=1$, $L/H=4$ (bottom).

of $G^{(k)}$ for $\delta \leqslant 1$ are less than 1, while for $\delta=10$ they are slightly higher.

Since both the BGK and S models provide identical results, up to three significant figures for most of the quantities under investigation, we do not use in the rest of the paper the superscript (k) in our notation. Also, when results on temperatures and heat fluxes are reported, they are based on the S model.

A more detailed description of the effect of the groove, which we will call "groove effect," on the behavior of the drag coefficient C_d and of the flow rate G is shown in Figs. 4 and 5, respectively, where the two quantities are plotted in terms of δ for three different geometrical configurations. We note that in Fig. 4, the drag coefficient C_d has been divided by the corresponding drag coefficient C_d^C of the one-dimensional Couette flow. By doing that, it is easier to study the effect of the presence of the groove on this quantity. Such a division is not necessary in Fig. 5, since the flow rate $G^C=1$ for all δ. At $\delta=0$, the ratio C_d/C_d^C takes its largest value and it is larger than 1. As δ is increased, the ratio of the drag coefficients is decreased. Depending upon the case, at about $1<\delta<5$ the ratio becomes equal to 1, while at $\delta=10$ it is always less than 1. The corresponding behavior of G is opposite. Overall, in all cases tested, we have found that $C_d>C_d^C$ and $G<1$ at small δ, while $C_d<C_d^C$ and $G>1$ at large δ.

From both figures, it is clearly seen that the groove effect becomes more dominant in rarefied atmospheres as δ is decreased. In addition, in terms of the width and the length of the groove, it is seen that the groove effect is increased as the ratio W/H is increased, while it is decreased as the ratio L/H is increased. Finally, in terms of the depth of the groove, as the ratio D/H is increased, first the groove effect is increased, then it reaches a maximum level at about $D/H=0.5$, and for $D/H>0.5$ it is reduced reaching a constant level at about $D/H=1$. Increasing further the depth of the groove has no effect on the values of C_d and G. These find-

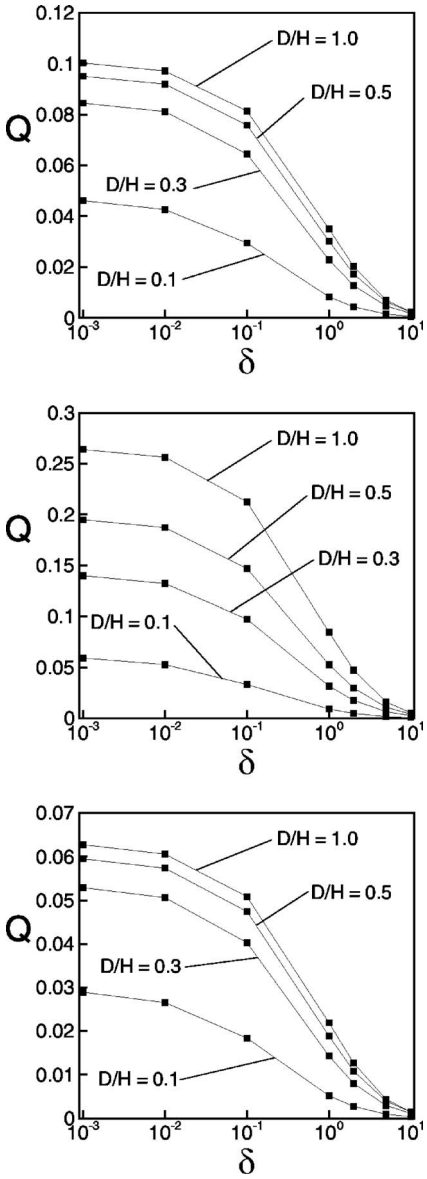

FIG. 6. Heat flux in terms of δ for various D/H with $W/H=1$, $L/H=2.5$ (top); $W/H=2$, $L/H=2.5$ (middle); and $W/H=1$, $L/H=4$ (bottom).

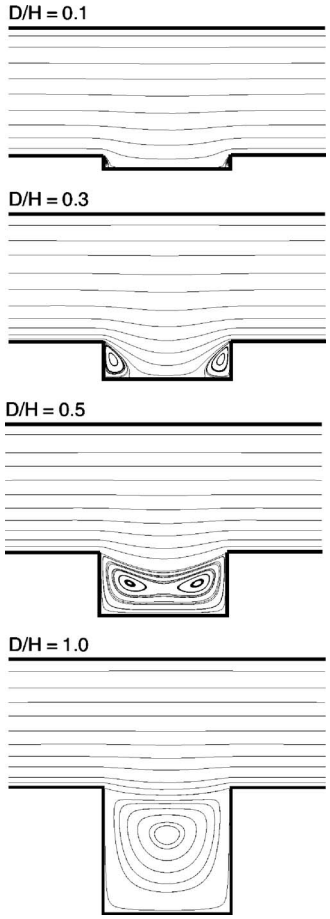

FIG. 7. Velocity streamlines for $\delta=1$, $W/H=1$, $L/H=2.5$, and various D/H.

ings have been verified by examining additional grooved channel flows with other geometric parameters.

In Fig. 6, the heat flux Q through the channel, defined by Eq. (14), is plotted in terms of δ for the same three geometrical configurations. It is noted that this quantity, in the one-dimensional Couette flow, is identically equal to zero. In all cases, the average heat flux has the maximum values at the free molecular limit and then it is decreased as δ is increased. At the continuum limit as δ goes to infinity, Q goes to zero. In terms of the geometric parameters, we note similar behavior as before with the exception that as the ratio D/H is increased, the groove effect on Q keeps increasing, reaching a maximum constant level when $D/H\sim 1$.

We continue by plotting in Figs. 7–9 velocity streamlines for several flow configurations. We keep the rarefaction parameter $\delta=1$, while we change the geometric parameters. In Fig. 7, the width and length ratios are $W/H=1$ and $L/H=2.5$, while the depth ratio is $D/H=0.1$, 0.3, 0.5, and 1. It is seen that as D/H is increased, vortices are created at the two bottom corners of the groove, which grow and merge into a primary vortex under the main flow. Additional vortices under the primary one may be obtained if the depth of the groove is increased further. This vortex creation mechanism has been described in detail recently in Ref. 30 studying the classical cavity flow problem in the whole range of the Knudsen number. Here, similar flow patterns and characteristics are observed inside the groove due to the motion of the fluid above the groove. For $D/H=0.1$, the depth of the groove is very small compared to the distance between the plates and therefore the effect of the groove on the main flow is not important. As the depth is increased, the influence of the groove on the main stream is increased until the two

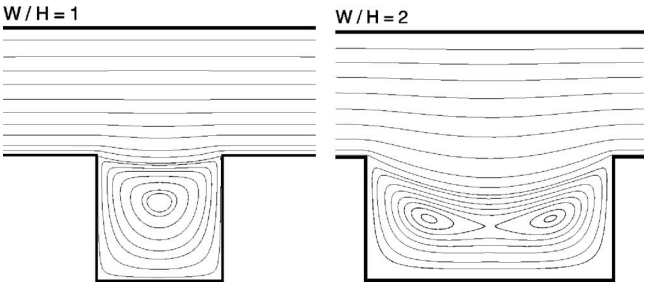

FIG. 8. Velocity streamlines for $\delta=1$, $D/H=1$, and $L/H=2.5$, with $W/H=1$ (left) and $W/H=2$ (right).

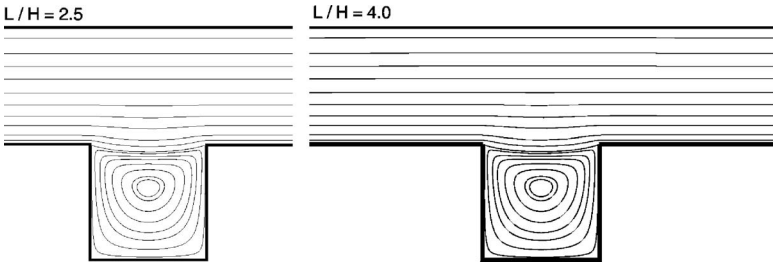

FIG. 9. Velocity streamlines for $\delta=1$, $D/H=1$, and $W/H=1$, with $L/H=2.5$ (left) and $L/H=4$ (right).

corner vortices merge and the main flow is no longer in touch with the bottom of the groove. In this particular flow configuration, the separation of the main flow from the bottom wall occurs at $0.3<D/H<0.5$. Then, for higher values of D/H, although additional vortices below the main one may be created, the influence of the groove on the main flow is decreased and the flow becomes progressively stratified, consisting of an upper channel flow and a groove recirculating vortex flow, with very small interaction between them. The two flows are distinguished by a thin shear layer. It is seen that the more drastic effect due to the presence of the groove on the flow pattern occurs at $D/H\sim0.3$, where the streamlines of the main flow bend and penetrate inside the cavity.

Velocity streamlines for different width and length ratios are presented in Figs. 8 and 9, respectively. In Fig. 8, the width ratio is $W/H=1$ and 2, while the depth and length ratios are $D/H=1$ and $L/H=2.5$. In Fig. 9, the length ratio is $L/H=2.5$ and 4, while the depth and width ratios are $D/H=1$ and $W/H=1$. It is clearly seen that changing the width of the groove has a much more significant impact on the flow pattern than changing the periodic length of the channel. By comparing the results in Figs. 7–9, it may be concluded that between the geometric parameters of the flow, the one that most influences the groove effect is the ratio W/H, followed by the ratio D/H, while the ratio L/H is the less important. These remarks can also be deduced by comparing the results in Figs. 4–6.

Velocity streamlines for various values of the rarefaction parameter δ, with $D/H=0.5$, $W/H=1$, and $L/H=2.5$, are shown in Fig. 10. It is seen that the qualitative differences in the streamline patterns between the various values of δ are small. In all cases, the groove vortex becomes more well developed as δ is increased.

The above described observations and findings, regarding the groove effect in terms of the rarefaction and the geometric parameters of the flow, agree in a qualitative manner with the ones found in Ref. 26, where both plates of the grooved channel were stationary and the flow was due to pressure and temperature gradients.

Typical contours of the perturbed density, pressure, and temperature for $\delta=1$, with $D/H=1$, $W/H=1$, and $L/H=2.5$, are shown in Fig. 11. All perturbation profiles are antisymmetric about $x=0$, where they vanish. They also vanish at $x=\mp L/2H$, while they are negative at $-L/2H<x<0$ and positive at $0<x<L/2H$. The pressure and density perturbations have the same order, while the temperature variation is smaller by at least one order of magnitude. In addition, the perturbations of all three quantities are very close to zero in the upper channel flow, while inside the groove they depart from zero. The most significant deviations from zero are observed along the side (vertical) walls of the groove. In particular, large negative and positive perturbations occur along the left and right walls of the groove, respectively, taking their maximum absolute values at the two top groove edges. Similar results have been obtained for other values of the rarefaction and geometric parameters. In general, as δ is increased and we are moving from the free molecular to the continuum regime, the perturbations in density, pressure, and temperature are reduced. In all cases, the linearized equation of state, given by Eq. (11), is fulfilled.

We close this section by providing for a specific geometry plots of $u_x(x,y)$, which is the x component of the velocity profile, at several cross sections along the channel. This

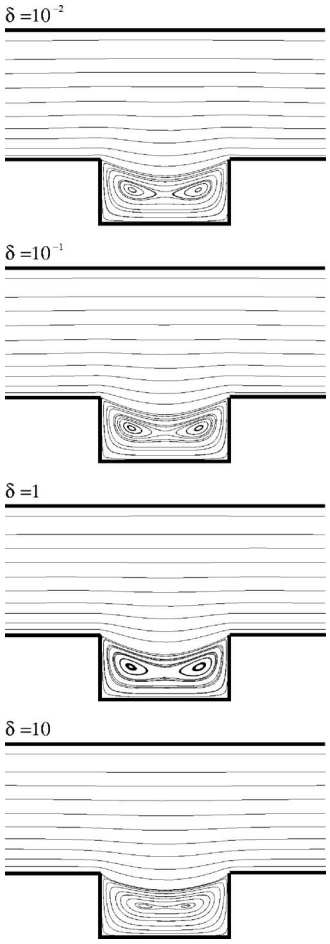

FIG. 10. Velocity streamlines for various δ, with $D/H=0.5$, $W/H=1$, and $L/H=2.5$.

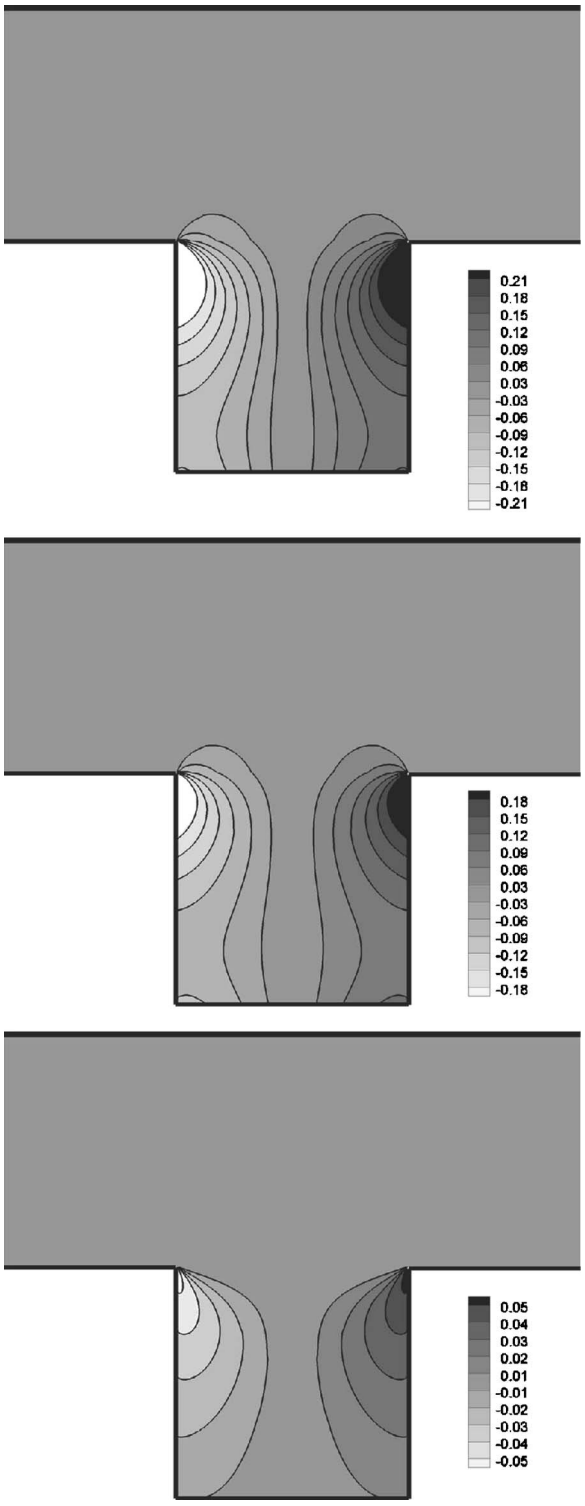

FIG. 11. Contours of pressure (top), density (middle), and temperature (bottom) for $\delta=1$, $D/H=1$, $W/H=1$, and $L/H=2.5$.

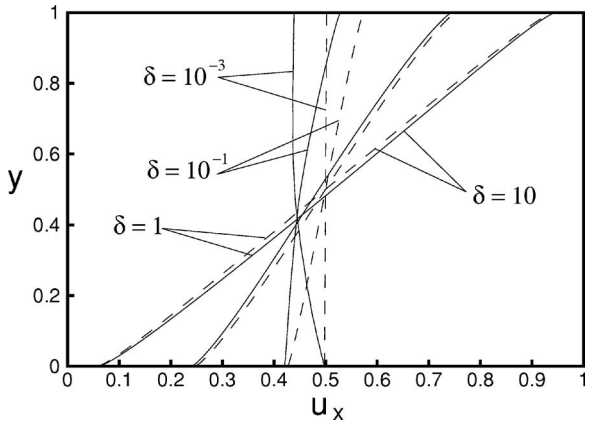

FIG. 12. Horizontal velocity profiles $u_x(x,y)$ at $x=-L/(2H)$ for various δ, with $D/H=0.5$, $W/H=1$, and $L/H=2.5$ (2D grooved channel flow, solid lines; 1D Couette flow, dashed lines).

quantity is symmetric about $x=0$. Results are presented for various values of δ, while the geometric parameters are $D/H=0.5$, $W/H=1$, and $L/H=2.5$.

In Fig. 12, the x component of the velocity distribution is plotted at the inlet $x=-L/2H$ of the channel, for $\delta=10^{-3}$, 10^{-1}, 1, and 10. The corresponding velocity profiles for the one-dimensional Couette flow are also included. For $\delta=10$, it is seen that the profiles with and without groove are very close. The magnitude of the velocity distribution corresponding to the grooved channel is slightly higher, resulting in a slightly higher flow rate (see also Table I or Table II and Fig. 5). This behavior may be explained by taking into account the fact that in the grooved channel flow, the interface between the main stream and the cavity may be considered as a moving boundary, while the corresponding boundary in the one-dimensional Couette flow is stationary. As the rarefaction is increased and δ is decreased, the situation is quite different. Now, the magnitude of the x component of the velocity distribution of the grooved channel is smaller than the corresponding distribution for the one-dimensional Couette flow, resulting in a smaller flow rate (see also Table I or Table II and Fig. 5). In addition, we note that for $\delta=10^{-1}$ and 10^{-3}, the velocities at the upper wall ($y=1$) are lower than expected. It may be useful to remark that the expected values of velocity at the upper wall are for $\delta=10^{-1}$ well above 0.5 and for $\delta=10^{-3}$ about 0.5. Even more interesting is the fact that for $\delta=10^{-3}$ the velocity at the upper moving wall ($y=1$) is lower than the velocity at the lower stationary wall ($y=0$). This unexpected finding, which is not consistent with physical intuition, is due to the rarefaction of the flow combined with the presence of the groove and it is mathematically and physically justified in the next section.

In order to have a complete picture of the evolution of the x component of the velocity distribution along the channel, in Fig. 13 additional profiles are provided at $x=-W/2H$ and along the symmetry axis of the grooved channel at $x=0$.

Before we conclude this section, it is useful to recall that due to linearization, the whole analysis is valid for slow flows (low Re and Ma numbers). Taking into account the relation $\mathrm{Re}\sim\delta\mathrm{Ma}$, the above restriction implies that for $\delta\leqslant 1$, the condition $U_0/v_0\ll 1$ is adequate, while for $\delta>1$ the required condition becomes $\delta U_0/v_0\ll 1$.

V. APPROXIMATE ESTIMATION OF THE VELOCITY AT THE UPPER WALL

It is well known that as the flow becomes more rarefied, it is dominated by collisions between particles and bound-

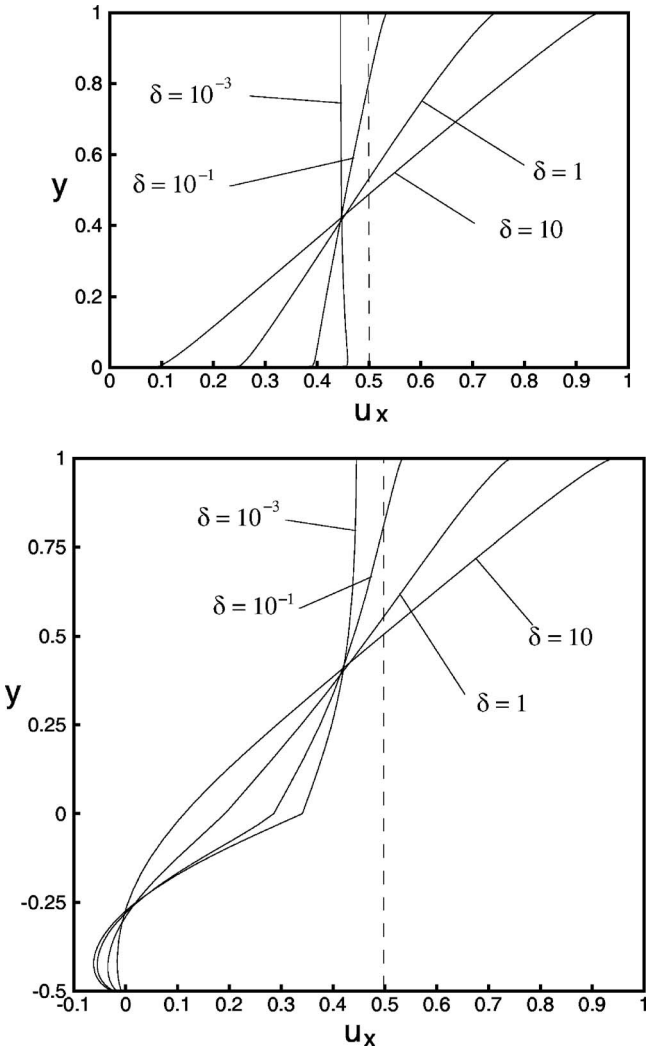

FIG. 13. Horizontal velocity profiles $u_x(x,y)$ at $x=-W/2H$ (top) and $x=0$ (bottom) for various δ, with $D/H=0.5$, $W/H=1$, and $L/H=2.5$.

aries, while collisions between particles are rare. In these cases, the distribution functions of the particles emitted from the boundaries have a dominant influence on the bulk quantities of the flow, including of course the macroscopic velocity.

For simplicity and demonstration purposes, let us assume that there is only one groove in the channel and let us consider the limiting case of free molecular flow ($\delta=0$). This flow configuration with the coordinate system and its origin is shown in Fig. 14. Trying to find the x component of the velocity at any point A, located along the upper moving wall (see Fig. 14), we write

$$u_x(A) = \frac{1}{\pi}\int_0^{2\pi}\int_0^{\infty} \phi\mu^2 e^{-\mu^2}\cos\theta d\mu d\theta$$
$$= \frac{1}{\pi}\int_0^{\infty}\mu^2 e^{-\mu^2}\left[\sum_{p=1}^{5}\int_{\theta_p}^{\theta_{p+1}}\phi_p\cos\theta d\theta + \int_{\pi}^{2\pi}\phi_6\cos\theta d\theta\right]d\mu. \quad (55)$$

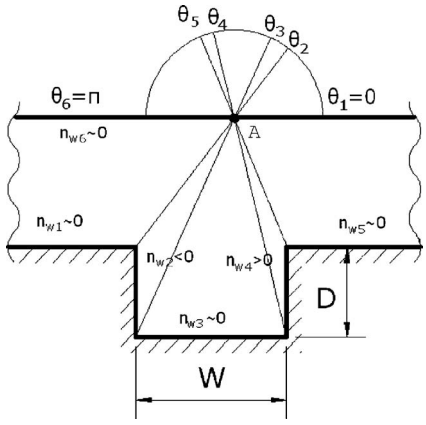

FIG. 14. Estimation of u_x along the upper plate.

The angles θ_p, with $\theta_1=0$ and $\theta_6=\pi$, are shown in Fig. 14, while ϕ_p are the distribution functions defined at each interval $\Delta\theta_p=\theta_{p+1}-\theta_p$. It is seen that the distributions $\phi_p, p=1,\ldots,5$ defined in the interval $(0,\pi)$ correspond to particles arriving at point A, while the distribution ϕ_6 defined in the interval $[\pi,2\pi]$ corresponds to particles departing from point A. Since we are assuming free molecular flow, the unknowns $\phi_p, p=1,\ldots,5$, are equal to the distributions emitted by the section of the stationary wall, which is facing the angle $\Delta\theta_p$, and we have

$$\phi_p = n_{wp} \quad p=1,\ldots,5. \quad (56)$$

The distribution ϕ_6, is known from the boundary condition at the upper moving wall and it is

$$\phi_6 = n_{w6} + 2\mu\cos\theta. \quad (57)$$

The parameters n_{wp}, $p=1,\ldots,6$, are defined at the corresponding walls as indicated in Fig. 14, and they are computed by applying the impermeability condition. We note that from these parameters, the ones that are defined along the horizontal walls of the grooved channel (i.e., n_{w1}, n_{w3}, n_{w5}, and n_{w6}) are very small and they may be assumed identically equal to zero.

Then, we substitute Eqs. (56) and (57) into Eq. (55), and after some manipulation and by taking into account the previous approximation, we readily find

$$u_x(A) = \frac{1}{2} + K + L, \quad (58)$$

where

$$K = \frac{1}{4\sqrt{\pi}} n_{w2}(\sin\theta_3 - \sin\theta_2) \quad \text{and}$$

$$L = \frac{1}{4\sqrt{\pi}} n_{w4}(\sin\theta_5 - \sin\theta_4). \quad (59)$$

Since always $n_{w2}<0$ and $n_{w4}>0$, it is deduced from Eq. (59) that, for any point A along the upper wall, both quantities K and L are always negative and as a result $u_x(A)<0.5$. Next, we follow exactly the same procedure, with the same assumptions as before, for any point B, at $y=0$, along the lower

stationary wall. Now, the whole procedure becomes much simpler since these points are not facing any section of the groove of the channel. It is readily deduced that $u_x(B)=0.5$. Therefore, we have shown, in a simplified mathematical manner, that in the case of free molecular flow, the magnitude of the x component of the velocity at the upper moving wall takes lower values than at the lower stationary wall. It is useful to recall that in the case of one-dimensional Couette flow, when $\delta=0$, both values are equal to 0.5.

From a physical point of view, one may argue that this phenomenon occurs due to the negative and positive variation of the perturbed densities (or pressures) of the gas along the left and right side walls of the groove, respectively. This variation, which becomes significant in highly rarefied atmospheres, has a dominant effect on the bulk velocity of the regions of the flow domain, which, due to geometry, are directly facing particles emitted from the side walls of the groove. It is obvious that this is true for the flow region, which is close to the upper plate, and as a result the bulk velocities in this region are lower than the flow velocities in the region close to the lower plate, which again due to geometry is less affected by the distribution functions of the particles emitted from the side walls of the grooves.

This analysis, which has been presented for $\delta=0$, can be extended and it is valid for $\delta>0$, as long as the flow is sufficiently rarefied ($\delta<1$). As δ is further increased and the flow is dominated by collisions between particles, the distributions of particles emitted at the side walls of the groove fade out quickly due to collisions and they can never reach the upper channel flow. As a result, this phenomenon is not present when the flow is sufficiently dense ($\delta>1$). This analysis is also valid in the case of the periodically grooved channel.

VI. CONCLUDING REMARKS

The flow of a rarefied gas in a grooved channel due to the motion of the upper plate has been investigated implementing a kinetic approach. The BGK and S kinetic equations, associated with suitable boundary conditions, have been solved by the discrete velocity method. In most cases, both models provide identical results, while when heat fluxes are computed, the S model is considered as more accurate. Detailed results have been computed, in several geometric configurations of the grooved channel, for the drag coefficient, the flow rate, and the heat flux. The corresponding flow patterns have been presented by plotting the velocity streamlines. Distributions of velocity and shear stress and contours of pressure, density, and temperature have been provided as well. The results are valid in the whole range of the rarefaction parameter δ.

By comparing the grooved channel flow with the one-dimensional Couette flow, the effect of the groove on the flow quantities and characteristics has been extensively investigated. It has been found that as the rarefaction of the flow is increased, the groove effect is also increased. In addition, between the geometric parameters of the flow it has been found that altering the width of the groove has the most significant impact, followed by the depth of the groove and the periodic length of the channel. In the case of highly rarefied flows ($\delta<1$), an unexpected phenomenon with regard to the velocity distributions across the channel has been observed and properly justified.

ACKNOWLEDGMENTS

The authors are grateful to Professor Felix Sharipov for several helpful discussions regarding this work. Partial support by the Hellenic Ministry of Education through the Program on Basic Research "Pythagoras" is gratefully acknowledged.

[1] J. M. Reese, M. A. Gallis, and D. A. Lockerby, "New direction in fluid mechanics, non-equilibrium aerodynamic and microsystem flows," Philos. Trans. R. Soc. London, Ser. A **361**, 2967 (2003).
[2] G. E. Karniadakis and A. Beskok, *Microflows: Fundamentals and Simulations* (Springer-Verlag, Berlin, 2000).
[3] A. Beskok, G. E. Karniadakis, and W. Trimmer, "Rarefaction and compressibility effects in gas microflows," ASME Trans. J. Fluids Eng. **118**, 448 (2006).
[4] H. Wang, P. Iovenitti, E. Harvey, and S. Massod, "Numerical investigation of mixing in microchannels with patterned grooves," J. Micromech. Microeng. **13**, 801 (2003).
[5] W. Sugiyama, T. Sawada, and K. Nakamori, "Rarefied gas flow between two flat plates with two dimensional surface roughness," Vacuum **47**, 791 (1996).
[6] H. Sun and M. Faghri, "Effect of surface roughness on nitrogen flow in a microchannel using direct simulation Monte Carlo method," Numer. Heat Transfer, Part A **43**, 1 (2003).
[7] H. P. Cheng, R. Y. Jou, F. Z. Chen, Y. W. Chang, M. Iwane, and T. Hanaoka, "Three-dimensional flow analysis of spiral-grooved turbo booster pump in slip and continuum flow," J. Vac. Sci. Technol. A **18**, 543 (2000).
[8] J.-S. Heo and Y.-K. Hwang, "Molecular transition and slip flows in the pumping channels of drag pumps," J. Vac. Sci. Technol. A **18**, 1025 (2000).
[9] O. Boulon and R. Mathes, "Flow modelling of a Holweck pump stage in the viscous regime," Vacuum **60**, 73 (2001).
[10] G. F. Naterer, P. S. Glockner, D. Thiele, S. Chomokovski, G. Venn, and G. Richardson, "Surface micro-grooves for near-wall exergy and flow control: Application to aircraft intake de-icing," J. Micromech. Microeng. **15**, 501 (2005).
[11] G. A. Bird, *Molecular Gas Dynamics and the Direct Simulation of Gas Flows* (Oxford University Press, Oxford, 1994).
[12] M. Gad-el Hak, *The MEMS Handbook* (CRC, Boca Raton, FL, 2002).
[13] J. H. Ferziger and H. G. Kaper, *Mathematical Theory of Transport Processes in Gases* (North-Holland, Amsterdam, 1972).
[14] C. Cercignani, *The Boltzmann Equation and Its Application* (Springer, New York, 1988).
[15] F. Sharipov and V. Seleznev, "Data on internal rarefied gas flows," J. Phys. Chem. Ref. Data **27**, 657 (1998).
[16] Y. Sone, *Kinetic Theory and Fluid Mechanics* (Birkhäuser, Boston, 2002).
[17] F. M. Sharipov and E. A. Subbotin, "On optimization of the discrete velocity method used in rarefied gas dynamics," ZAMP **44**, 572 (1993).
[18] D. Valougeorgis and S. Naris, "Acceleration schemes of the discrete velocity method: Gaseous flows in rectangular microchannels," SIAM J. Sci. Comput. (USA) **25**, 534 (2003).
[19] S. Naris, D. Valougeorgis, D. Kalempa, and F. Sharipov, "Gaseous mixture flow between two parallel plates in the whole range of the gas rarefaction," Physica A **336**, 294 (2004).
[20] S. Naris, D. Valougeorgis, F. Sharipov, and D. Kalempa, "Flow of gaseous mixtures through rectangular microchannels driven by pressure, temperature and concentration gradients," Phys. Fluids **17**, 100607 (2005).
[21] S. Naris and D. Valougeorgis, "Shear driven microflows of gaseous mixtures," Sens. Lett. **4**, 1 (2006).

[22] Y. Sone, Y. Waniguchi, and K. Aoki, "One-way flow of a rarefied gas induced in a channel with a periodic temperature distribution," Phys. Fluids **8**, 2227 (1996).
[23] Y. Sone and K. Sato, "Demonstration of a one-way flow of a rarefied gas induced through a pipe without average pressure and temperature gradients," Phys. Fluids **12**, 1864 (2000).
[24] K. Aoki and P. Degond, "Homogenization of a flow in a periodic channel of small section," Multiscale Model. Simul. **1**, 304 (2003).
[25] K. Yamamoto, H. Takeuchi, and T. Hyakutake, "Effect of surface grooves on the rarefied gas flow between two parallel walls," in *24th Rarefied Gas Dynamics* (API, Bari, 2005).
[26] S. Naris and D. Valougeorgis, "Gas flow in a grooved channel due to pressure and temperature gradients," in *Proceedings of the 4th International Conference on Nanochannels, Microchannels and Minichannels*, ICNMM2006 (2006), Vol. 2006A, pp. 539–546.
[27] F. Sharipov, P. Fahrenbach, and A. Zipp, "Numerical modelling of the Holweck pump," J. Vac. Sci. Technol. A **23**, 1331 (2005).
[28] N. K. Ghaddar, K. Z. Korczak, B. B. Mimic, and A. T. Patera, "Numerical investigation of incompressible flow in grooved channels. Part 1: Stability and self-sustained oscillations," J. Fluid Mech. **163**, 99 (1986).
[29] X. Wan and G. E. Karniadakis, "Stochastic heat transfer enhancement in a grooved channel," J. Fluid Mech. **565**, 255 (2006).
[30] S. Naris and D. Valougeorgis, "The driven cavity flow over the whole range of the Knudsen number," Phys. Fluids **17**, 097106 (2005).
[31] P. L. Bhatnagar, E. P. Gross, and M. Krook, "A model for collision processes in gases. I. Small amplitude processes in charged and neutral one-component systems," Phys. Rev. **94**, 511 (1956).
[32] P. Welander, "On the temperature jump in a rarefied gas," Ark. Fys. **7**, 507 (1954).
[33] E. M. Shakhov, "Generalization of the Krook kinetic relaxation equation," Fluid Dyn. **3**, 95 (1968).
[34] S. Naris, D. Valougeorgis, F. Sharipov, and D. Kalempa, "Discrete velocity modelling of gaseous mixture flows in MEMS," Superlattices Microstruct. **35**, 629 (2004).